PREPRINT

Enhancing the formation of ionic defects to study the ice Ih/XI transition with molecular dynamics simulations

Pablo M. Piaggi[a] and Roberto Car[b]

[a]Department of Chemistry, Princeton University, Princeton, NJ 08544, USA;
[b]Department of Chemistry and Department of Physics, Princeton University, Princeton, NJ 08544, USA

ABSTRACT
Ice Ih, the common form of ice in the biosphere, contains proton disorder. Its proton-ordered counterpart, ice XI, is thermodynamically stable below 72 K. However, even below this temperature the formation of ice XI is kinetically hindered and experimentally it is obtained by doping ice with KOH. Doping creates ionic defects that promote the migration of protons and the associated change in proton configuration. In this article, we mimic the effect of doping in molecular dynamics simulations using a bias potential that enhances the formation of ionic defects. The recombination of the ions thus formed proceeds through fast migration of the hydroxide and results in the jump of protons along a hydrogen bond loop. This provides a physical and expedite way to change the proton configuration, and to accelerate diffusion in proton configuration space. A key ingredient of this approach is a machine learning potential trained with density functional theory data and capable of modeling molecular dissociation. We exemplify the usefulness of this idea by studying the order-disorder transition using an appropriate order parameter to distinguish the proton environments in ice Ih and XI. We calculate the changes in free energy, enthalpy, and entropy associated with the transition. Our estimated entropy agrees with experiment within the error bars of our calculation.

1. Introduction

By 1933 there was a growing body of evidence that calorimetric and spectroscopic determinations of the entropy of water did not agree with each other[1, 2]. The crucial assumption of calorimetric measurements (later to be proven wrong) was that the third law of thermodynamics was valid for ice, i.e. at 0 K the entropy of ice had to be zero. It was also known from x-ray diffraction experiments that oxygen atoms in ice had the structure that we now call hexagonal diamond with each oxygen tetrahedrally coordinated[3]. However, Bernal and Fowler[4] had pointed out in 1933 that it was conceivable that the orientation of water molecules in ice could be random while maintaining the periodic arrangement of oxygen atoms in the lattice. They thus proposed the ice rules stating that, even in presence of disorder in the molecular orientations, each pair of oxygen nearest neighbors share only one hydrogen atom, and each oxygen atom has two strongly bonded and two weakly bonded hydrogen atoms. The next step forward came from Pauling[5] in 1935 who made a famous back-of-the-envelope

CONTACT Pablo M. Piaggi. Email: ppiaggi@princeton.edu

calculation showing that the disorder of hydrogen atoms (protons) gave rise to a residual entropy in good agreement with the entropy inferred from spectroscopy. Pauling's calculation reconciled spectroscopic and calorimetric measurements, and bolstered the hypothesis that ice had proton disorder. Later, his estimate of the entropic contribution from proton disorder was subject to several refinements(*6*, *7*). The solid form of water that we have so far simply referred to as ice, is nowadays called ice Ih since a large number of other ice polymorphs have since been discovered.

A proton ordered counterpart of ice Ih is a consequence of the third law of thermodynamics, yet for many years there was no experimental confirmation of its existence. In the context of the study of the dielectric properties of ice, Bjerrum(*8*), Onsager(*9*), and others realized that strict adherence to the ice rules could kinetically hinder changes in proton configuration. They then proposed mechanisms that could alter the proton configuration due to the presence of defects that locally violate the ice rules. These defects are the Bjerrum and ionic defects (OH^- and H_3O^+). Onsager also surmised that doping ice with HF could increase the number of ionic and Bjerrum defects, and thus facilitate this process(*10*). Tajima et al. showed in 1982 that it was possible to obtain a ferroelectric proton-ordered form by doping ice with KOH instead of HF(*11*). Subsequently, the structure of the proton ordered form was completely determined(*12*) and the polymorph is now called ice XI. This polymorph is now believed to be more stable than ice Ih below 72 K at ambient pressure(*11*).

Molecular simulations are a useful tool to obtain microscopic insight into physicochemical phenomena and several works have been devoted to the study of the ice Ih/XI transition. Many of these aimed at calculating the residual entropy of ice Ih using structurally accurate models in combination with simplified energy models(*13*, *14*). The subtle variation of energy of different proton configurations has been studied by Buch *et al.* using a polarizable water potential(*15*) and by Singer *et al.* using density-functional theory (DFT) and graph invariants(*16*). Sampling proton configurations in realistic molecular simulations is difficult as these simulations suffer from the same limitation of experiments regarding the kinetic hindrance of changes in proton configuration. In a pioneering simulation of ice in 1972, Rahman and Stillinger devised an algorithm to change the proton configuration by displacing protons along hydrogen-bond loops(*17*). This type of algorithm has often been used in the context of Monte Carlo simulations(*18–21*). Recently, Lasave *et al.* have studied the ice Ih/XI transition using replica-exchange Monte Carlo simulation of a spin-like Hamiltonian explicitly introducing ionic defects(*22*).

Here, we aim at studying the ice Ih/XI transition within molecular dynamics simulations. Our work contains at least two elements of novelty. First, we employ a machine learning potential trained with density-functional theory data. Therefore our model is able to describe the subtle variation in energy between different proton configurations and also the dissociation of the water molecule. Second, we employ enhanced sampling methods in order to accelerate changes in proton configuration. Our approach is based on the introduction of a bias potential that promotes the formation of oxygen atoms with three-fold proton coordination. This procedure leads to proton jumps along hydrogen-bond loops that result in changes of the proton configuration. At variance with other approaches, our method does not create permanent ionic defects in the structure of ice. We then take advantage of the enhanced diffusion in proton configuration space to study the ice Ih/XI transition using an order parameter tailored for that purpose.

2. Methods

2.1. *Machine learning model for water*

One of the fundamental ingredients of our approach is a model of water able to describe the self-ionization and the proton transfer process. We employ a machine learning model of water[23] built using the DeePMD framework[24, 25]. The model is based on deep neural networks and was trained with density functional theory (DFT) data obtained by adopting the strongly constrained and appropriately normed (SCAN) functional. Further details of the model are provided in ref. [23].

We used systems of 96 water molecules. Simulations were performed in the isothermal-isobaric ensemble and we employed a timestep of 0.5 fs. The temperature was kept constant using the stochastic velocity rescaling thermostat with a relaxation time of 0.1 ps. The pressure was maintained at 1 bar using an anisotropic Parrinello-Rahman barostat. Even though the sides of the box were allowed to change, the angles were fixed at 90°. All simulations were performed using the molecular dynamics engine LAMMPS[26] driven by the DeePMD-kit[27].

2.2. *Enhanced sampling using a variational principle*

In this work we focus on two processes: the formation of ionic defects and the change in proton configuration to drive the transformation from ice Ih to ice XI. These processes are rare events in the scale of a molecular dynamics simulation and we thus have to resort to techniques to accelerate them. Enhanced sampling methods aim at increasing the probability to observe rare but crucial fluctuations. Here we take advantage of the variationally enhanced sampling (VES) method introduced by Valsson and Parrinello[28]. This method is similar in spirit to umbrella sampling[29] or metadynamics[30, 31], and is based on the introduction of a bias potential $V(\mathbf{s})$ that is a function of a set of collective variables (CVs) $\mathbf{s}$. The CVs are continuous and differentiable functions of the atomic coordinates $\mathbf{R}$ and are chosen to describe the evolution of the process under study. At the core of the VES method is a functional of $V(\mathbf{s})$, and it can be shown that the minimum of this functional is reached for

$$V(\mathbf{s}) = -F(\mathbf{s}) - \frac{1}{\beta} \log p(\mathbf{s}), \tag{1}$$

where $F(\mathbf{s}) = -(1/\beta) \log \int d\mathbf{R}\, \delta(\mathbf{s} - \mathbf{s}(\mathbf{R})) e^{-\beta[U(\mathbf{R}) + \mathcal{P}\mathcal{V}]}$ is the free energy, β is the inverse temperature, $U(\mathbf{R})$ is the potential energy, $\mathcal{P}$ is the pressure, $\mathcal{V}$ is the volume, and $p(\mathbf{s})$ is the target probability distribution of the CVs. $p(\mathbf{s})$ has to be chosen properly in order to surmount free energy barriers and increase the probability of observing rare configurations. Typical choices of $p(\mathbf{s})$ are the uniform distribution $p(\mathbf{s}) = \text{const}$ and the well-tempered distribution[32, 33] $p(\mathbf{s}) = P(\mathbf{s})^{1/\gamma}$ where $\gamma \geq 1$ is the bias factor and $P(\mathbf{s}) = \int d\mathbf{R}\, \delta(\mathbf{s} - \mathbf{s}(\mathbf{R})) e^{-\beta[U(\mathbf{R}) + \mathcal{P}\mathcal{V}]}$ is the unbiased distribution of the CVs.

In practice, one has to expand the bias potential in basis functions and the expansion parameters are determined using an algorithm akin to stochastic gradient descent. Further details can be found in ref. [28]. We employed Legendre polynomials and the well-tempered target distribution. Multiple walkers were used to improve the convergence of the bias potential. The PLUMED enhanced sampling plugin[34–36] was used in tandem with LAMMPS in order to determine and apply the bias potential.

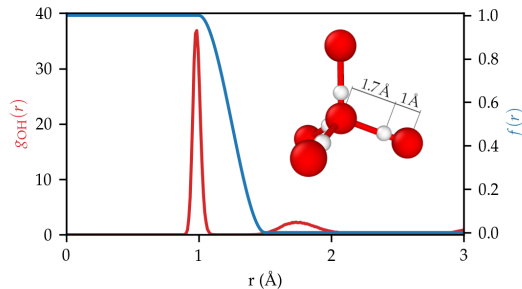The bias potential alters the probability of observing a given configuration, and

3

Figure 1. Radial distribution function $g_{\text{OH}}(r)$ between oxygen and hydrogen atoms and switching function $f(r)$ used to calculate the coordination number of hydrogen with oxygen. The environment around an oxygen atom shows a case in which the ice rules are satisfied, i.e. there are two hydrogen atoms at ~ 1 Å and another two hydrogen atoms at ~ 1.7 Å. Therefore the coordination number computed using $f(r)$ is ~ 2 in this case. Oxygen and hydrogen atoms shown in red and white, respectively.

therefore the calculation of observables requires special attention. A thorough discussion on the calculation of observables using the reweighting technique has been given in refs. (*37–39*).

2.3. *Collective variable to enhance the formation of ionic defects*

The simplest ionic defects are the hydronium H_3O^+ and hydroxide OH^- ions. More complex entities such as the Zundel ion $H_5O_2^+$ and the Eigen ion $H_9O_4^+$ are also possible, which, however, represent only limiting or ideal structures(*40*). In order to promote the formation of these defects it seems natural to consider the coordination number of each oxygen with hydrogen.

The coordination number of the $i-$th oxygen is,

$$n_i = \sum_{j \in \text{H}} f(r_{ij}), \tag{2}$$

where r_{ij} is the norm of the distance between oxygen atom i and hydrogen atom j, and $f(r_{ij})$ is a continuous and differentiable switching function that is one at short distance and zero at distances larger than some radius r_{max}. For our simulations we have chosen,

$$f(y) = \begin{cases} 1 & \text{if} \quad y < 0 \\ (y-1)^2(1+2y) & \text{if} \quad 0 < y < 1 \\ 0 & \text{if} \quad y > 1 \end{cases}, \tag{3}$$

where $y = (r - r_0)/(r_{max} - r_0)$, r_0 is a distance below which all hydrogen atoms are considered neighbors, and beyond the distance r_{max} all hydrogen atoms are ignored. For the model studied here, the first and second peaks of the O-H radial distribution function $g_{\text{OH}}(r)$ are located at around 1 and 1.7 Å as shown in Figure 1. These peaks correspond to the two strongly bonded and two weakly bonded protons considered in the ice rules (see oxygen environment in Figure 1). Based on this information we have used $r_0 = 1$ Å and $r_{max} = 1.5$ Å. The switching function $f(r)$ based on this choice is shown in Figure 1. Therefore, $n_i \approx 2$ if the ice rules are satisfied.

By promoting changes in the coordination number we will create local deviations

4

from the ice rules. We now consider the number of oxygen atoms that have a coordination number larger than two. This is equivalent to the number of oxygen atoms with three-fold hydrogen coordination since coordination numbers larger than three were not observed. Thus, we use the notation N_{H_3O}. This quantity can be written as,

$$N_{H_3O} = \sum_{i \in O} \theta(n_i - n_0) \tag{4}$$

where $\theta(n_i - n_0)$ is a characteristic function such that $\theta(n_i - n_0) = 0$ if $n_i < n_0$ and $\theta(n_i - n_0) = 1$ if $n_i > n_0$. We choose $n_0 = 2.5$ in order to count the number of oxygen atoms that have a coordination number larger than two. N_{H_3O} can also be made continuous and differentiable by replacing $\theta(n_i - n_0)$ by a suitable switching function,

$$N_{H_3O} = \sum_{i \in O} \frac{x^p - x^q}{1 - x^q}, \tag{5}$$

where N is the total number of oxygen atoms, $x = n_i/n_0$, and the exponents p and q control the steepness of the switching function. The choice $p = 24$, $q = 48$ provides a good compromise between a clear separation of oxygen atoms with $n_i = 2$ and $n_i = 3$, and a smooth transition from zero to one in the switching function. We shall use this definition of N_{H_3O} as a collective variable in the VES formalism to promote the formation of ionic defects with excess protons. The formation and subsequent migration of the ionic defects will lead to changes in proton configuration.

2.4. *Collective variable to drive the ice Ih/XI transition*

Now that we have discussed how to promote changes in proton configuration, we turn our attention to the transformation of ice Ih into ice XI. In this section we describe an order parameter that distinguishes ice Ih from ice XI. Both polymorphs share the same structure of the oxygen atoms yet differ in the position of the protons. The positions of the protons in ice XI are uniquely defined since it is an ordered structure. However, the hexagonal diamond structure of the oxygen sublattice has four different environments (the number of molecules in the primitive cell of ice Ih is four) and we will have to characterize each of them. Furthermore, ferroeletric ice XI has two possible orientations with opposite dipole moments within the same sublattice of oxygen atoms. This results from the mirror symmetry with respect to the basal plane. The symmetry between the two possible orientations leads to spontaneous symmetry breaking, i.e. the two states are degenerate and the system will choose one of them during the transformation.

In order to describe the local structure of ice XI we shall use four environments $X^\uparrow = \{\chi_1^\uparrow, \chi_2^\uparrow, \chi_3^\uparrow, \chi_4^\uparrow\}$ for the up orientation ($\uparrow$) of the dipole moment, and four environments $X^\downarrow = \{\chi_1^\downarrow, \chi_2^\downarrow, \chi_3^\downarrow, \chi_4^\downarrow\}$ for the down orientation ($\downarrow$). These environments are shown in Figure 2. Using these environments we can construct a similarity measure(*41*) using a similarity kernel(*42*). This type of similarity measure has been used to study the crystallization of simple metals(*42*), of ice Ih(*38*), and of several polymorphs of gallium(*43*). We restrict the following discussion to the $\uparrow$ variant of ice XI although the same discussion applies to the $\downarrow$ variant. We define the kernel between the four
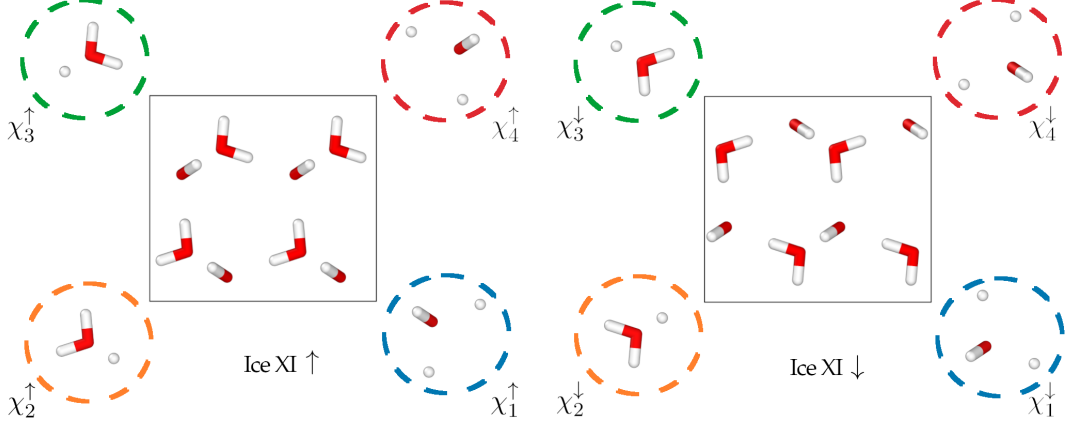
5

Figure 2. Environments around oxygen atoms in ice XI. There are four environments $X^\uparrow = \{\chi_1^\uparrow, \chi_2^\uparrow, \chi_3^\uparrow, \chi_4^\uparrow\}$ for the up orientation ($\uparrow$) of the dipole moment, and four environments $X^\downarrow = \{\chi_1^\downarrow, \chi_2^\downarrow, \chi_3^\downarrow, \chi_4^\downarrow\}$ for the down orientation ($\downarrow$) of the dipole moment.

reference environments $\chi_l^\uparrow \in X^\uparrow$ and a generic environment χ,

$$k_{\chi_l^\uparrow}(\chi) = \int \rho_{\chi_l^\uparrow}(\mathbf{r})\rho_\chi(\mathbf{r})\, d\mathbf{r}, \tag{6}$$

where $\rho_{\chi_l^\uparrow}(\mathbf{r})$ and $\rho_\chi(\mathbf{r})$ are the atomic densities corresponding to the environments $\chi_l^\uparrow$ and χ, respectively. We shall represent the density using sums of Gaussians with spread σ, centered at the neighbors' positions, and rewrite the kernel as:

$$k_{\chi_l^\uparrow}(\chi) = \frac{1}{n} \sum_{i\in\chi_l^\uparrow} \sum_{j\in\chi} \exp\left(-\frac{|\mathbf{r}_i^l - \mathbf{r}_j|^2}{4\sigma^2}\right), \tag{7}$$

where n is the number of neighbors in the environment $\chi_l^\uparrow$, and $\mathbf{r}_i^l$ and $\mathbf{r}_j$ are the positions of the neighbors in environments $\chi_l^\uparrow$ and χ, respectively. In Eq. (7) we have included a normalization such that $k_{\chi_l^\uparrow}(\chi_l) = 1$. Now we have four similarity kernels that allow us to identify whether a given environment is compatible with one of the four proton environments in ice XI. A similarity measure between a given environment and any of the four proton environments in the $\uparrow$ variant of ice XI is,

$$k_{X^\uparrow}(\chi) = \max\{k_{\chi_1^\uparrow}(\chi), k_{\chi_2^\uparrow}(\chi), k_{\chi_3^\uparrow}(\chi), k_{\chi_4^\uparrow}(\chi)\}. \tag{8}$$

In Figure 3 we show the distribution of $k_{X^\uparrow}(\chi)$ and $k_{X^\downarrow}(\chi)$ in ice Ih, ice XI $\uparrow$, and ice XI $\downarrow$ at 300 K. Since ice Ih can have any environment compatible with the ice rules, there is a variety of environments that give rise to three peaks in the distribution of $k_{X^\uparrow}(\chi)$ and $k_{X^\downarrow}(\chi)$. This is expected since Ih might contain some of the environments that exist in ice XI. The interpretation of the distribution in ice XI is straightforward. In ice XI $\uparrow$ the kernel $k_{X^\uparrow}(\chi)$ recognizes all environments as compatible with those of ice XI $\uparrow$ and the kernel $k_{X^\downarrow}(\chi)$ founds little or no similarity with the environments of ice XI $\uparrow$. The converse is true for the distributions in ice XI $\downarrow$.
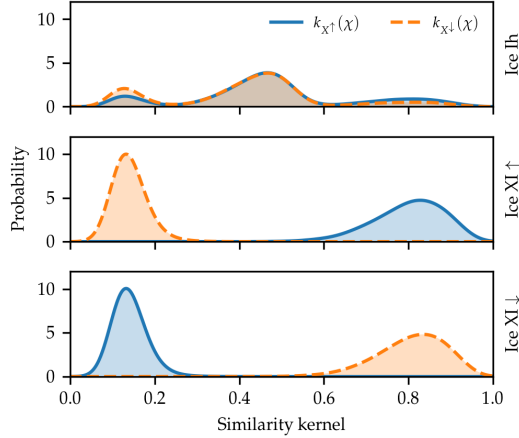
Figure 3. Distribution of the similarity kernels $k_{X\uparrow}(\chi)$ and $k_{X\downarrow}(\chi)$ in ice Ih, ice XI $\uparrow$, and ice XI $\downarrow$ at 300 K.

These kernels characterize the environment around a single atom. However, for a system with N water molecules there will be N oxygen-hydrogen environments $\chi^1, \chi^2, ..., \chi^N$. We consider the average value of the kernel,

$$\bar{k}^\uparrow = \frac{\sum_{i=1}^{N} k_{X\uparrow}(\chi^i)}{N}, \tag{9}$$

and the number of environments consistent with the $\uparrow$ variant of ice XI,

$$n_{\mathrm{XI}}^\uparrow = \{\text{number of } \chi^i \ : \ k_{X\uparrow}(\chi^i) > \kappa\}, \tag{10}$$

where κ is a threshold separating the values of $k_{X\uparrow}(\chi^i)$ consistent with ice Ih and those consistent with ice XI.

These global order parameters are restricted to one of the variants of ice XI. We can also define an order parameter akin to the one used in Landau's theory of phase transitions(44),

$$\bar{k} = \bar{k}^\uparrow - \bar{k}^\downarrow \tag{11}$$

that satisfies $\bar{k} \approx 0$ in ice Ih (the disordered phase), $\bar{k} > 0$ in the $\uparrow$ variant of ice XI, and $\bar{k} < 0$ in the $\downarrow$ variant of ice XI. This order parameter is able to distinguish the two variants of ice XI. However, both variants are equivalent by symmetry and therefore thermodynamic properties, such as, e.g. the free energy, as a function of $\bar{k}$ must be even functions. It is convenient to include this symmetry in the order parameter using

$$|\bar{k}| = |\bar{k}^\uparrow - \bar{k}^\downarrow| \tag{12}$$

that satisfies $|\bar{k}| \approx 0$ in ice Ih, and $|\bar{k}| > 0$ in ice XI. We shall see that better resolution of the local changes in structure can be achieved using

$$|n_{\mathrm{XI}}| = |n_{\mathrm{XI}}^\uparrow - n_{\mathrm{XI}}^\downarrow|. \tag{13}$$

7

It is easy to see that $|n_{\mathrm{XI}}| \approx 0$ in ice Ih, and $|n_{\mathrm{XI}}| \approx N$ in ice XI. We will use a continuous and differentiable version of n_{XI} to construct a bias potential with the VES framework (see reference (38) for details).

3. Results and discussion

We performed a 1 ns long unbiased molecular dynamics simulation of ice XI at 300 K. In Figure 4 we show the number of H_3O-like defects in the system as a function of simulation time. The number of H_3O-like defects can be calculated using Eq. (5) and replacing $f(r)$ with a step function at 1.25 Å. We observed that the number of H_3O-like defects remained close to zero throughout the simulation, implying that the ice rules were always satisfied and that no ionic defects were spontaneously created.

We then introduced a bias potential as a function of the collective variable N_{H_3O} defined in Eq. (5). The bias potential was optimized to target the well-tempered distribution with bias factor 50. After 250 ps the bias was quasi-static, well-converged and the system explored a number of H_3O-like defects varying from zero to around ten as shown in Figure 4. An inspection of the proton configuration at around 750 ps after the bias potential was introduced, shows that the ordered proton configuration of ice XI has changed to a disordered configuration (see snapshot in Figure 4). We also observed that the defects created by the bias potential are not isolated H_3O-like entities but rather they involve larger numbers of oxygen atoms along hydrogen bond loops or strings (see snapshot in Figure 4). From the simulation we can also compute the free energy associated with the creation of different numbers of H_3O-like defects. The formation of a single H_3O defect has a free energy cost of around 30 kJ/mol. This free energy should not be confused with the formation free energy of a H_3O^+ - OH^- pair, since in this case the two ions must be well separated.

We now turn to study the mechanism by which changes in proton configuration are achieved. To this end we analyzed the first proton jumps along a hydrogen-bond loop observed during the biased simulation. This event is shown with snapshots of the system's configuration in Figure 5. Initially, the proton configuration is ordered and corresponds to ice XI. After 7.5 ps there are fluctuations that promote the sharing of a proton by two oxygen atoms, yet there is not a clear spatial separation of charge in the system. The change in proton configuration is triggered at 14 ps by the formation of an $H_7O_3^+$ cation and an OH^- anion that leads to the first proton jump and charge separation. Further proton jumps occur in the next few ps as the OH^- propagates along a hydrogen bond chain. After the initial proton jump, the $H_7O_3^+$ seems to transform into a $H_5O_2^+$ (Zundel) cation. However, the initial formation of the $H_7O_3^+$ cation does not seem to be crucial since in other events we observed only the Zundel ion. The snapshot at 18.25 ps shows evidence of collective behavior in the diffusion of the OH^- anion since at least three water molecules seem to be involved in a concerted proton jump. At 19.5 ps no ion is observed along this hydrogen-bond loop, but a new pair of Zundel and OH^- has formed elsewhere in the simulation box. Further events follow a similar mechanism. While most proton jumps are a consequence of the diffusion of the OH^- anion, the diffusion of the Zundel cation results in two proton jumps. A total of 16 proton jumps occur in a time span of around 5.5 ps. We also analyzed the displacement of the protons and found that after 1 ns around 60 % of the protons have been displaced from their original positions.

The analysis above implies a higher mobility of the OH^- ion than of the H_3O^+ ion in ice Ih. As a matter of fact, we can calculate the ratio of the diffusion coeffi-
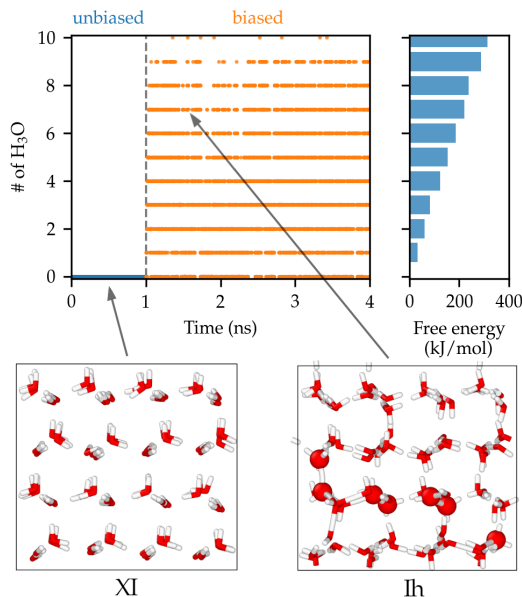
Figure 4. Number of H_3O-like defects as a function of simulation time. After 1 ns of unbiased simulation, a bias potential is introduced to enhance the formation of ionic defects. Trajectories of four multiple walkers are concatenated for the biased portion of the results. The free energy as a function of the number of H_3O-like defects is also shown. The initial ice XI configuration is shown below and the proton ordered structure can be seen. After 750 ps of biased simulation the configuration shows proton disorder compatible with ice Ih. Oxygen atoms are shown in red and hydrogen atoms are shown in white. H_3O defects are shown with red spheres.

cients from the limited number of jumps described above to be $D_{OH^-}/D_{H_3O^+} \approx 6$. This result would be in stark contrast with the situation in liquid water. There is significant evidence that the diffusion of H_3O^+ in liquid water is almost two times faster than the diffusion of OH^-(45, 46), i.e. $D_{OH^-}/D_{H_3O^+} \approx 0.5$. This behavior in liquid water has been attributed to a stabilized hypercoordinated solvation structure around OH^-(47, 48). In ice Ih the formation of such a structure is not allowed as a consequence of the crystalline structure of oxygen atoms. As far as we know, to date there is no experimental evidence that $D_{OH^-} > D_{H_3O^+}$ in ice. The availability of data on the diffusion coefficient of OH^- and H_3O^+ in ice is limited compared to corresponding data for liquid water(49). The limited data is a result of experimental difficulties, and the fact that the charge transport in ice supposedly involves not only the ionic defects OH^- and H_3O^+, but also the Bjerrum L and D defects(49). As a result of these issues, the estimations of the steady-state conductivity and of the diffusion coefficients of ionic defects can vary over several orders of magnitude(49). From the event that we have analyzed, we can also calculate approximately the jump frequencies and diffusion coefficients of OH^- and H_3O^+ that we report in Table 1. Onsager and Dupuis(9) estimated the sum of the jump frequencies, but their result relies on disputed measurements of the steady-state conductivity(49).

The phase transformation from ice XI to ice Ih entails a change in the total dipole moment. However, flipping all protons along a hydrogen bond loop contained in the simulation box, conserves the dipole moment of the system. In our simulations we observe also winding loops, i.e. loops that end in a different periodic image of the system. Flipping protons along winding loops does change the total dipole moment and allows the system to undergo the ice XI/Ih transition. Even though real systems do not have periodic boundary conditions, one can surmise a similar mechanism for changes
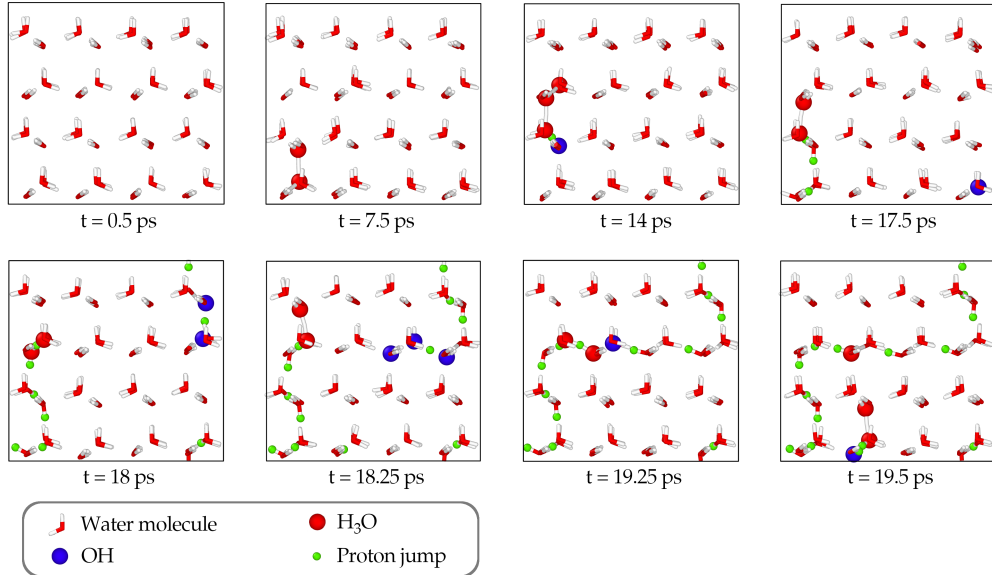
9

Figure 5. Sequence of configurations that illustrate the mechanism by which changes in proton configurations are achieved. Oxygen and hydrogen atoms are shown in red and white, respectively. H_3O and OH defects are shown with red and blue spheres. Protons that have jumped with respect to their initial configurations are shown in green.

in proton configuration in real systems provided that there are internal surfaces or defects that can act as sources and sinks of ionic defects.

We can also use the order parameter $\bar{k}$ defined in Eq. (11) to analyze the change from the ordered proton configuration of ice XI to a disordered proton configuration. In Figure 6 we show $\bar{k}$ as a function of simulation time in a biased simulation starting from ice XI and another one starting from ice Ih. The biased simulation that starts from ice Ih has a $\bar{k} \sim 0$ throughout the simulation in spite of the changes in proton configuration. On the other hand, the biased simulation that starts from the $\uparrow$ variant of ice XI has an initial value of around $\bar{k} \sim 0.65$ but within 200 ps reaches $\bar{k} \sim 0$ and preserves that value throughout the rest of the simulation. An unbiased simulation would show no changes in $\bar{k}$ since no changes in proton configurations occur in this case.

The analysis in Figure 6 shows also that promoting changes in the proton configuration by itself does not suffice to observe reversible transitions between ice Ih and ice XI. For this reason, we introduced another bias potential using VES and $|n_{XI}|$ as CV. In Figure 7 we show $|n_{XI}|$ as a function of time at 200, 250, and 300 K. The bias potential allows the system to explore reversibly ordered and disordered proton configurations. $|n_{XI}| \sim 0$ corresponds to ice Ih and $|n_{XI}| \sim 96$ corresponds to ice XI. The number of transitions between the ordered and disordered proton configurations

Table 1. Jump frequency ν and diffusion coefficient D of ionic defects at 300 K (based on very limited information of one $OH^- $-$H_3O^+$ recombination event). The diffusion coefficient is calculated using the formula $D = \nu d^2/6$ with $d = 2.76$ Å the interoxygen distance.

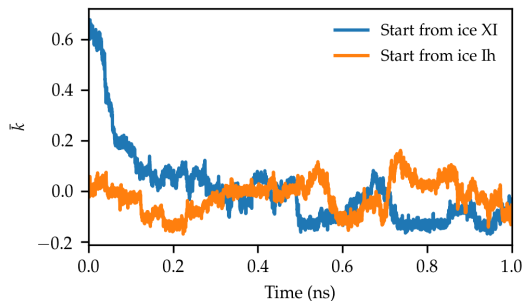|	ν (ps^{-1})	D (10^{-8} m^2/s)
OH^-	~ 2.5	~ 3.2
H_3O^+	~ 0.4	~ 0.5
$OH^- + H_3O^+$	~ 2.9	~ 3.7

10

Figure 6. Order parameter $\bar{k}$ as a function of simulation time at 300 K. The biased simulation that starts from the ↑ variant of ice XI evolves to a disorder proton structure compatible with ice Ih after around 200 ps. $\bar{k}$ in the biased simulation starting from ice Ih does not see appreciable changes in its value.
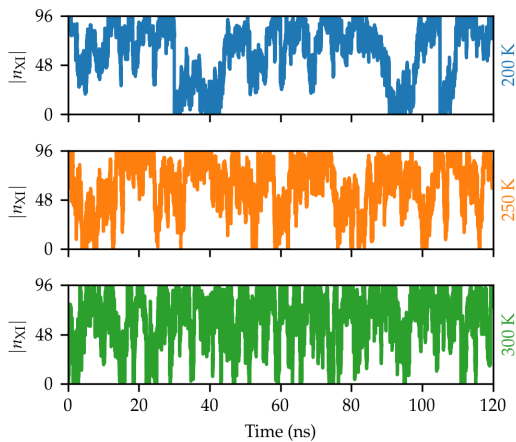

Figure 7. Order parameter $|n_{\mathrm{XI}}|$ as a function of simulation time. Simulations at 200, 250, and 300 K are shown. The trajectories of eight multiple walkers were concatenated to make the plots.

falls sharply as the temperature is lowered from 300 K to 200 K. We attribute the drop in the number of transitions to the slower creation of ionic defects at low temperature. For this reason we did not study lower temperatures. It is possible that changing the definition of the switching functions used to define the collective variables could help to further enhance the creation of ionic defects. An approach like parallel tempering(*50*) could also be used to study lower temperatures.

From the simulations described above we can calculate the free energy as a function of $\bar{k}$ and n_{XI} using reweighting. These functions are plotted in Figure 8 and bear similarity to Landau free energy profiles above the critical temperature. We have enforced the even parity of the free energy required by symmetry. The minimum of the free energy is located at $n_{\mathrm{XI}} \sim 0$ and $\bar{k} \sim 0$. Thus, ice Ih is the most stable phase at the temperatures studied here. In the free energy as a function of $\bar{k}$ there is a shallow minimum at around $|\bar{k}| \sim 0.7$ that corresponds to ice XI. This minimum is shifted to higher values of $|\bar{k}|$ as the temperature is lowered as a consequence of reduced thermal fluctuations. On the other hand, in the free energy as a function of n_{XI} the ice XI minimum is precisely located at $|n_{\mathrm{XI}}| = 96$ at all temperatures. Furthermore, there is a barrier that separates ice XI from other proton configurations that was not observed when $\bar{k}$ was used as order parameter. For this reason, we conclude that n_{XI} provides a greater resolution of the proton configurations in our simulation. The existence of a barrier separating the two phases is also the hallmark of a first order phase transition,
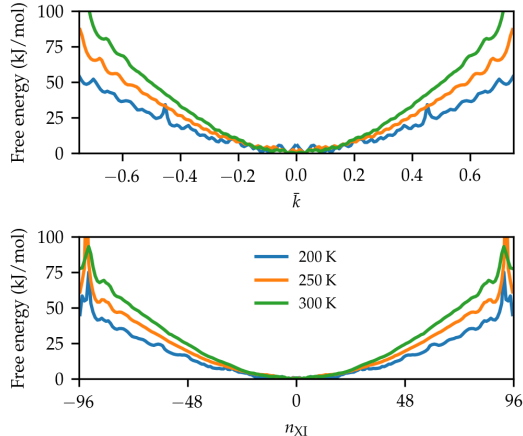
11

Figure 8. Free energy as a function of the order parameters $\bar{k}$ and n_{XI}.

and there is experimental evidence that the transformation is indeed of first order(*12*). There are also systematic shallow minima that cannot be ascribed to the statistical uncertainty. These minima are located at $|n_{\mathrm{XI}}| \sim 80$ and $|\bar{k}| \sim 0.6$. A visual inspection of the configurations shows that they correspond to ordered layers of protons that are likely stabilized by the periodic boundary conditions used in the simulations.

We also calculated the difference in chemical potential $\mu_{\mathrm{XI}} - \mu_{\mathrm{Ih}}$ and enthalpy $H_{\mathrm{XI}} - H_{\mathrm{Ih}}$ between ice XI and Ih using reweighting. The results are shown as a function of temperature in Figure 9. Although our calculations were performed at relatively high temperature, we can extrapolate the results at low temperatures by fitting a straight line to $\mu_{\mathrm{XI}} - \mu_{\mathrm{Ih}}$. Based on this extrapolation we obtain a transition temperature of around 50 K for the machine learning model based on the SCAN functional employed here. $H_{\mathrm{XI}} - H_{\mathrm{Ih}}$ seems fairly independent of the temperature and has an average value of 180 J/mol. This difference in enthalpy is in good agreement with the experimental result 168 J/mol from calorimetric measurements(*51*). We also calculated $H_{\mathrm{XI}} - H_{\mathrm{Ih}}$ at 0 K by an energy minimization with respect to the atomic coordinates and the box tensor, and obtained $H_{\mathrm{XI}} - H_{\mathrm{Ih}} = 230$ J/mol. Using this value for the enthalpy and a theoretical estimate for the residual entropy of 0.410 k_B (*6*), a somewhat higher transition temperature of 67.5 K is obtained. The agreement with the experimental value of 72 K is particularly good for the latter estimate.

From the thermodynamic relation $\Delta S = (\Delta H - \Delta G)/T$ we can also calculate the entropy. In Figure 9 we show the residual entropy S_0 at the three temperatures studied here. The residual entropy is independent of temperature within error bars, and the mean value is $S_0 = 0.417(6)$ k_B if only the simulations at 250 and 300 K are considered. This value can be compared with the result of Pauling's (*5*) mean-field calculation $S_0 = 0.405$ k_B, Nagle's(*6*) calculation $S_0 = 0.410$ k_B using a series expansion method that takes into account some hydrogen-bond loops(*7*), and the experimental result(*5*) $S_0 = 0.41(3)$ k_B. We note that Pauling's result is a lower bound for S_0 (*9*), while Nagle's result is an improvement over Pauling's calculation yet neglects energy effects. Our calculation includes energy effects but is affected by the finite size of the system. Finite size effects tend to increase the residual entropy as shown by Herrero and Ramirez(*14*) and Berg *et al.*(*13*), and for this reason our calculation is an upper bound for S_0 We stress that our result agrees with the experiment within the error bars.
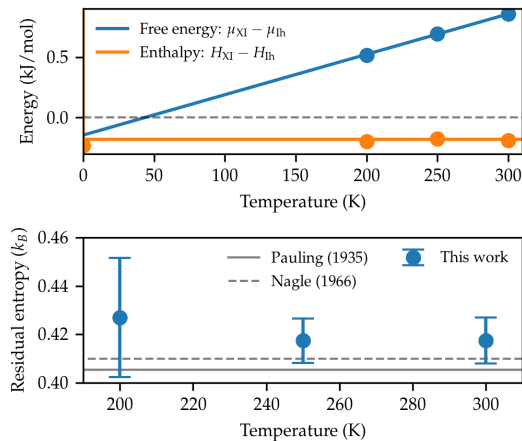
Figure 9. Above) Difference in chemical potential $\mu_{\mathrm{XI}} - \mu_{\mathrm{Ih}}$ and enthalpy $H_{\mathrm{XI}} - H_{\mathrm{Ih}}$ between ice XI and Ih. The lines were fit to the data at 200, 250, and 300 K. We have included the enthalpy at 0 K calculated from structure optimizations of ice XI and Ih. Below) Difference in entropy between ice XI and Ih (residual entropy) calculated from the simulations at difference temperatures. Estimations due to Pauling(5) and Nagle(6) are also shown.

4. Conclusions

We presented a method to accelerate changes in proton configurations in molecular dynamics simulations based on introducing a bias potential that promotes the formation of ionic defects. This approach provides an alternative to the Monte Carlo algorithm often used to sample proton configurations(17–19). We analyzed the mechanism of the changes in proton configuration. We found that the initial charge separation in the system is a result of the formation of an $H_7O_3{}^+$ or $H_5O_2{}^+$ (Zundel) cation, and a OH^- anion. After the charge separation, most proton jumps along a hydrogen bond loop are a result of the diffusion of the OH^- anion. We also found evidence of collective behavior in the diffusion of the OH^- anion with at least three water molecules involved in a concerted proton jump. Finally, the two ionic defects recombine and all the protons in the hydrogen bond loop remain flipped. Changes in the total dipole moment are allowed as a consequence of the periodic boundary conditions that gives rise to winding loops.

We also showed the usefulness of this approach by studying the ice XI/Ih transition. For this purpose, we constructed an *ad hoc* order parameter for ice XI based on the local atomic environments around oxygen atoms. An appropriate quasi-static bias potential as a function of this order parameter sufficed to drive reversible transitions between ice XI and ice Ih. From these simulations we calculated the free energy difference between the two phases and the residual entropy of ice Ih. We obtained a residual entropy of $0.417(6)$ k_B that is in agreement with the experiment within the error bar of our calculation. We argue that it represents an upper bound to the true residual entropy since finite size effects reduce the residual entropy. As far as we know, this is the first calculation of the residual entropy that fully takes into account the subtle variation in energy between different proton configurations. The approximate transition temperature obtained here from an extrapolation of high temperature simulations is around 50 K. Statistical errors affect this extrapolation as well as size effects, thus it should be considered a rough estimate. This temperature is lower than the experimental transition temperature, 72 K, and also lower than the simple estimate of 67.5

13

K that can be obtain from static calculations of the enthalpy at 0 K for this model.

Our approach was made possible by the use of a machine learning potential based on the SCAN exchange and correlation functional. This model is able to describe the dissociation of water and therefore the proton transfer between oxygen atoms. We found that this model reproduces well the higher stability of ice XI than of Ih at 0 K, and also the ice XI/Ih transition temperature is in reasonable agreement with experiment. We note that these results depend on the choice of the level of theory used for training the NNP, and that the potential energy surface (PES) described by our model is not a perfect representation of the SCAN PES(*52*). Furthermore, the potential employed here was not trained with configurations representative of the proton transfer process yet a similar model has been shown to describe these events reasonably well(*53*).

The performance of the method presented here to change the proton configuration deteriorates at low temperatures. Extending the usefulness of this approach to lower temperatures will be the subject of future work. Furthermore, the order parameter for the ice XI/Ih introduced here can find multiple applications. For instance, it could be used to mimic the effect of an electric field acting on the system. This would allow to perform a computer experiment in which the rearrangement of the proton configuration is driven by a simulated external electric field.

References

(1) Giauque, W.F.; Ashley, M.F. Molecular rotation in ice at 10 K. free energy of formation and entropy of water, *Physical review* **1933**, *43* (1), 81.

(2) Giauque, W.; Stout, J. The Entropy of Water and the Third Law of Thermodynamics. The Heat Capacity of Ice from 15 to 273 K., *Journal of the American Chemical Society* **1936**, *58* (7), 1144–1150.

(3) Barnes, W.H. The crystal structure of ice between 0 C. and—183 C, *Proceedings of the Royal Society of London. Series A, Containing Papers of a Mathematical and Physical Character* **1929**, *125* (799), 670–693.

(4) Bernal, J.D.; Fowler, R.H. A theory of water and ionic solution, with particular reference to hydrogen and hydroxyl ions, *The Journal of Chemical Physics* **1933**, *1* (8), 515–548.

(5) Pauling, L. The structure and entropy of ice and of other crystals with some randomness of atomic arrangement, *Journal of the American Chemical Society* **1935**, *57* (12), 2680–2684.

(6) Nagle, J.F. Lattice statistics of hydrogen bonded crystals. I. The residual entropy of ice, *Journal of Mathematical Physics* **1966**, *7* (8), 1484–1491.

(7) DiMarzio, E.; Stillinger Jr, F. Residual entropy of ice, *The Journal of Chemical Physics* **1964**, *40* (6), 1577–1581.

(8) Bjerrum, N. Structure and properties of ice, *Science* **1952**, *115* (2989), 385–390.

(9) Onsager, L.; Dupuis, M. The electrical properties of ice, *Rend. Sc. Int. Fis. "Enrico Fermi"* **1960**, *10*, 294–315.

(10) Onsager, L.; Weller, E. Ferroelectricity of ice, *Ferroelectricity. Elsevier, Amsterdam* **1967**, 16–19.

(11) Tajima, Y.; Matsuo, T.; Suga, H. Phase transition in KOH-doped hexagonal ice, *Nature* **1982**, *299* (5886), 810–812.

(12) Line, C.M.; Whitworth, R. A high resolution neutron powder diffraction study of D2O ice XI, *The Journal of chemical physics* **1996**, *104* (24), 10008–10013.

(13) Berg, B.A.; Muguruma, C.; Okamoto, Y. Residual entropy of ordinary ice from multi-canonical simulations, *Physical Review B* **2007**, *75* (9), 092202.

(14) Herrero, C.P.; Ramírez, R. Configurational entropy of ice from thermodynamic integration, *Chemical Physics Letters* **2013**, *568*, 70–74.

(15) Buch, V.; Sandler, P.; Sadlej, J. Simulations of H2O Solid, Liquid, and Clusters, with an Emphasis on Ferroelectric Ordering Transition in Hexagonal Ice, *The Journal of Physical Chemistry B* **1998**, *102* (44), 8641–8653.

(16) Singer, S.J.; Kuo, J.L.; Hirsch, T.K.; Knight, C.; Ojamäe, L.; Klein, M.L. Hydrogen-bond topology and the ice VII/VIII and ice I h/XI proton-ordering phase transitions, *Physical review letters* **2005**, *94* (13), 135701.

(17) Rahman, A.; Stillinger, F.H. Proton distribution in ice and the Kirkwood correlation factor, *The Journal of Chemical Physics* **1972**, *57* (9), 4009–4017.

(18) Barkema, G.; Newman, M. Monte Carlo simulation of ice models, *Physical Review E* **1998**, *57* (1), 1155.

(19) Rick, S.W.; Haymet, A. Dielectric constant and proton order and disorder in ice Ih: Monte Carlo computer simulations, *The Journal of chemical physics* **2003**, *118* (20), 9291–9296.

(20) Rick, S.W. Simulations of proton order and disorder in ice Ih, *The Journal of chemical physics* **2005**, *122* (9), 094504.

(21) Schönherr, M.; Slater, B.; Hutter, J.; VandeVondele, J. Dielectric properties of water ice, the ice Ih/XI phase transition, and an assessment of density functional theory, *The Journal of Physical Chemistry B* **2014**, *118* (2), 590–596.

(22) Lasave, J.; Koval, S.; Laio, A.; Tosatti, E. Proton strings and rings in atypical nucleation of ferroelectricity in ice, *Proceedings of the National Academy of Sciences* **2020**, *118* (1).

(23) Gartner, T.E.; Zhang, L.; Piaggi, P.M.; Car, R.; Panagiotopoulos, A.Z.; Debenedetti, P.G. Signatures of a liquid–liquid transition in an ab initio deep neural network model for water, *Proceedings of the National Academy of Sciences* **2020**. `https://www.pnas.org/content/early/2020/10/01/2015440117`.

(24) Zhang, L.; Han, J.; Wang, H.; Car, R.; E, W. Deep potential molecular dynamics: a scalable model with the accuracy of quantum mechanics, *Physical review letters* **2018**, *120* (14), 143001.

(25) Zhang, L.; Han, J.; Wang, H.; Saidi, W.; Car, R.; E, W. End-to-end symmetry preserving inter-atomic potential energy model for finite and extended systems, *Advances in Neural Information Processing Systems* **2018**, *31*, 4436–4446.

(26) Plimpton, S. Fast parallel algorithms for short-range molecular dynamics, *Journal of computational physics* **1995**, *117* (1), 1–19.

(27) Wang, H.; Zhang, L.; Han, J.; E, W. DeePMD-kit: A deep learning package for many-body potential energy representation and molecular dynamics, *Computer Physics Communications* **2018**, *228*, 178–184.

(28) Valsson, O.; Parrinello, M. Variational approach to enhanced sampling and free energy calculations, *Physical review letters* **2014**, *113* (9), 090601. `https://link.aps.org/doi/10.1103/PhysRevLett.113.090601`.

(29) Torrie, G.M.; Valleau, J.P. Nonphysical sampling distributions in Monte Carlo free-energy estimation: Umbrella sampling, *Journal of Computational Physics* **1977**, *23* (2), 187–199.

(30) Laio, A.; Parrinello, M. Escaping free-energy minima, *Proceedings of the National*

Academy of Sciences **2002**, *99* (20), 12562–12566.

(31) Barducci, A.; Bussi, G.; Parrinello, M. Well-tempered metadynamics: A smoothly converging and tunable free-energy method, *Physical review letters* **2008**, *100* (2), 020603.

(32) Bonomi, M.; Parrinello, M. Enhanced sampling in the well-tempered ensemble, *Physical review letters* **2010**, *104* (19), 190601. `https://link.aps.org/doi/10.1103/PhysRevLett.104.190601`.

(33) Valsson, O.; Parrinello, M. Well-Tempered Variational Approach to Enhanced Sampling, *Journal of chemical theory and computation* **2015**, *11* (5), 1996–2002. `https://doi.org/10.1021/acs.jctc.5b00076`.

(34) Tribello, G.A.; Bonomi, M.; Branduardi, D.; Camilloni, C.; Bussi, G. PLUMED 2: New feathers for an old bird, *Computer Physics Communications* **2014**, *185* (2), 604–613.

(35) Bonomi, M.; Bussi, G.; Camilloni, C.; Tribello, G.A.; Banáš, P.; Barducci, A.; Bernetti, M.; Bolhuis, P.G.; Bottaro, S.; Branduardi, D.; et al. Promoting transparency and reproducibility in enhanced molecular simulations, *Nature methods* **2019**, *16* (8), 670–673.

(36) *VES Code*, a library that implements enhanced sampling methods based on Variationally Enhanced Sampling written by O. Valsson. For the current version, see http://www.ves-code.org, `http://www.ves-code.org`.

(37) Valsson, O.; Tiwary, P.; Parrinello, M. Enhancing Important Fluctuations: Rare Events and Metadynamics from a Conceptual Viewpoint, *Annual Review of Physical Chemistry* **2016**, *67* (1).

(38) Piaggi, P.M.; Car, R. Phase equilibrium of liquid water and hexagonal ice from enhanced sampling molecular dynamics simulations, *The Journal of Chemical Physics* **2020**, *152* (20), 204116.

(39) Invernizzi, M.; Piaggi, P.M.; Parrinello, M. Unified Approach to Enhanced Sampling, *Phys. Rev. X* **2020**, *10*, 041034.

(40) Marx, D.; Tuckerman, M.E.; Hutter, J.; Parrinello, M. The nature of the hydrated excess proton in water, *Nature* **1999**, *397* (6720), 601–604.

(41) Bartók, A.P.; Kondor, R.; Csányi, G. On representing chemical environments, *Physical Review B* **2013**, *87* (18), 184115.

(42) Piaggi, P.M.; Parrinello, M. Calculation of phase diagrams in the multithermal-multibaric ensemble, *The Journal of chemical physics* **2019**, *150* (24), 244119.

(43) Niu, H.; Bonati, L.; Piaggi, P.M.; Parrinello, M. Ab initio phase diagram and nucleation of gallium, *Nature Communications* **2020**, *11* (1), 1–9.

(44) Landau, L.D.; Lifshitz, E. *Statistical physics, part I*; pergamon, Oxford, 1980.

(45) Halle, B.; Karlström, G. Prototropic charge migration in water. part 2.—Interpretation of nuclear magnetic resonance and conductivity data in terms of model mechanisms, *Journal of the Chemical Society, Faraday Transactions 2: Molecular and Chemical Physics* **1983**, *79* (7), 1047–1073.

(46) Sluyters, J.; Sluyters-Rehbach, M. The mechanism of the hydrogen ion conduction in liquid light and heavy water derived from the temperature dependence of their limiting conductivities, *The Journal of Physical Chemistry B* **2010**, *114* (47), 15582–15589.

(47) Lee, S.H.; Rasaiah, J.C. Proton transfer and the mobilities of the H+ and OH- ions from studies of a dissociating model for water, *The Journal of chemical physics* **2011**, *135* (12), 124505.

(48) Chen, M.; Zheng, L.; Santra, B.; Ko, H.Y.; DiStasio Jr, R.A.; Klein, M.L.; Car, R.; Wu, X. Hydroxide diffuses slower than hydronium in water because its solvated structure inhibits correlated proton transfer, *Nature chemistry* **2018**, *10* (4), 413–419.

(49) Petrenko, V.F.; Whitworth, R.W. *Physics of ice*; OUP Oxford, 1999.

(50) Sugita, Y.; Okamoto, Y. Replica-exchange molecular dynamics method for protein folding, *Chemical physics letters* **1999**, *314* (1-2), 141–151.

(51) Tajima, Y.; Matsuo, T.; Suga, H. Calorimetric study of phase transition in hexagonal ice doped with alkali hydroxides, *Journal of Physics and Chemistry of Solids* **1984**, *45* (11-12), 1135–1144.

(52) Piaggi, P.M.; Panagiotopoulos, A.Z.; Debenedetti, P.G.; Car, R. Phase equilibrium of

water with hexagonal and cubic ice using the SCAN functional, *arXiv:2101.04806* **2021**.

(53) Andrade, M.F.C.; Ko, H.Y.; Zhang, L.; Car, R.; Selloni, A. Free energy of proton transfer at the water–TiO 2 interface from ab initio deep potential molecular dynamics, *Chemical Science* **2020**, *11* (9), 2335–2341.